

Boundary scattering in the ϕ^4 model

Patrick Dorey^a, Aliaksei Halavanau^{b,c}, James Mercer^a, Tomasz Romanczukiewicz^d
and Yasha Shnir^{b,e,f}

^a*Department of Mathematical Sciences, Durham University, UK*

^b*Department of Theoretical Physics and Astrophysics, Belarusian State University,
Minsk, Belarus*

^c*Department of Physics, Northern Illinois University, USA*

^d*Institute of Physics, Jagiellonian University, Krakow, Poland*

^e*BLTP, JINR, Dubna, Russia*

^f*Institute of Physics, Oldenburg University, Germany*

ABSTRACT: We study boundary scattering in the ϕ^4 model on a half-line with a one-parameter family of Neumann-type boundary conditions. A rich variety of phenomena is observed, which extends previously-studied behaviour on the full line to include regimes of near-elastic scattering, the restoration of a missing scattering window, and the creation of a kink or oscillon through the collision-induced decay of a metastable boundary state. We also study the decay of the vibrational boundary mode, and explore different scenarios for its relaxation and for the creation of kinks.

Contents

1	Introduction	1
2	The model	2
3	Numerical results	3
4	Kink-boundary forces and the location of the low-velocity window	5
5	The boundary mode	7
6	The resonance mechanism in boundary scattering	9
7	Radiative decay of the boundary mode	13
8	Higher-order nonlinear effects and amplitude-dependent decay rates	16
9	Creation of kinks from an excited boundary	18
10	Conclusions	20
A	Numerical methods	20
B	Supplementary material	21

1 Introduction

Systems with boundaries, defects and impurities have been intensively studied in statistical physics and field theory, both at the classical and the quantum levels. Often the key physics of the model can be captured, possibly after dimensional reduction, by a simple 1+1 dimensional field theory on a half line. Examples include the Kondo problem [1], fluxon propagation in long Josephson junctions [2], the XXZ model with boundary magnetic field [3], an impurity in an interacting electron gas [4], the sine-Gordon [5] and Toda [6] models, monopole catalysis [7], the Luttinger liquid [8], and a toy model motivated by M-theory [9].

Especially since the work of Ghoshal and Zamolodchikov [5], there has been great interest in boundary conditions compatible with bulk integrability, and many such models turn out to be of direct physical interest. However less attention has been paid to the equally if not more physically-relevant cases of non-integrable boundary systems, even at the classical level. This is perhaps a shame, as it is now known that non-integrable classical field theories, even in 1+1 dimensions, can exhibit remarkably rich patterns of behaviour not seen in their integrable counterparts [10–14].

In this paper we examine the ϕ^4 theory in 1+1 dimensions, restricted to a half line by a simple Neumann-type ‘magnetic field’ boundary condition. (The sine-Gordon model with a non-integrable boundary was recently investigated in [15].) The ϕ^4 theory on a full line is similar to the sine-Gordon model in that both support topological kinks and antikinks; the ϕ^4 theory also has an intriguing and still not fully-understood counterpart of the sine-Gordon breather, the oscillon [16]. We chose the magnetic field boundary condition in part because of its simplicity, and in part because the scattering of kinks against such a boundary provides a natural deformation of the full-line scattering problems which are already known to exhibit intricate patterns of resonant scattering [10–13]. In some regimes our results do indeed resemble the pattern of scattering windows observed in kink-antikink collisions on the full line, while in others we find novel phenomena including a new type of ‘sharp-edged’ scattering window. Even though the theory is not integrable, it turns out to be possible to give an accurate analytical description of some aspects of this behaviour. We complement these studies with an investigation of the decay of the vibrational boundary mode through nonlinear couplings to scattering states, and of the creation of kinks by an excited boundary. An interesting feature of the boundary mode decay, discussed in section 8, is that with suitable initial conditions a period of relatively slow decay can be followed by a sudden burst of radiation from the boundary as a new decay channel opens.

While this paper is self-contained, we have also made a number of short movies to illustrate aspects of the discussion, which can be found at [17]. After a brief explanation of the numerical methods used to obtain our plots in appendix A, these are listed in appendix B.

2 The model

We consider a rescaled ϕ^4 theory with vacua $\phi_v \in \{-1, +1\}$ on the left half-line $-\infty < x < 0$. The bulk energy and Lagrangian densities are $\mathcal{E} = \mathcal{T} + \mathcal{V}$ and $\mathcal{L} = \mathcal{T} - \mathcal{V}$ respectively, where

$$\mathcal{T} = \frac{1}{2}\phi_t^2 \quad \text{and} \quad \mathcal{V} = \frac{1}{2}\phi_x^2 + \frac{1}{2}(\phi^2 - 1)^2. \quad (2.1)$$

The static full-line kink and antikink, $\phi_K(x) = \tanh(x - x_0)$ and $\phi_{\bar{K}}(x) = -\phi_K(x)$, have rest mass $M = 4/3$ and interpolate between the two vacua. Including a boundary energy $-H\phi_0$, where $\phi_0 = \phi(0, t)$ and H can be interpreted as a boundary magnetic field, yields the Neumann-type boundary condition $\phi_x(0, t) = H$ at $x = 0$.

For $0 < H < 1$ there are four static solutions to the equations of motion, shown in figure 1. Two of them, $\phi_1(x) = \tanh(x - X_0)$ and $\phi_2(x) = \tanh(x + X_0)$ with $X_0 = \cosh^{-1}(1/\sqrt{|H|})$, are restrictions of regular full-line kinks to the half-line, while the other two, $\phi_3(x) = -\coth(x - X_1)$ and $\phi_4(x) = -\coth(x + X_1)$ with $X_1 = \sinh^{-1}(1/\sqrt{|H|})$ are irregular on the full line. On the half line, ϕ_3 is non-singular and corresponds to the absolute minimum of the energy, while ϕ_1 is metastable, and ϕ_2 is the unstable saddle-point between ϕ_3 and ϕ_1 . Their energies can be found by rewriting $E[\phi] = \int_{-\infty}^0 \mathcal{V} dx - H\phi_0$ in Bogomolnyi form as

$$E[\phi] = \frac{1}{2} \int_{-\infty}^0 (\phi_x \pm (\phi^2 - 1))^2 dx \mp \left[\frac{1}{3}\phi^3 - \phi \right]_{-\infty}^0 - H\phi_0. \quad (2.2)$$

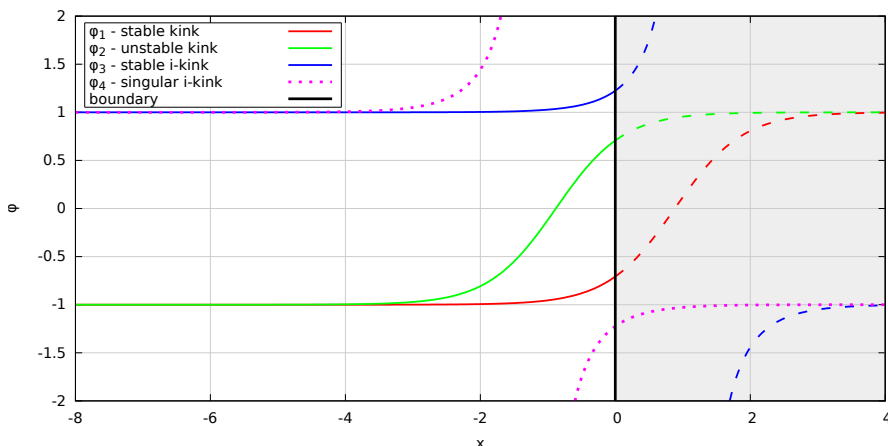


Figure 1. Static solutions for $H = 1/2$.

Since ϕ_1 and ϕ_2 satisfy $\phi_x = 1 - \phi^2$ we have $\phi_1(0) = -\sqrt{1-H}$, $\phi_2(0) = \sqrt{1-H}$; while $(\phi_3)_x = \phi_3^2 - 1$ and so $\phi_3(0) = \sqrt{1+H}$. Taking the upper and lower signs in (2.2) as appropriate,

$$\begin{aligned} E[\phi_1] &= \frac{2}{3} - \frac{2}{3}(1-H)^{3/2}, & E[\phi_2] &= \frac{2}{3} + \frac{2}{3}(1-H)^{3/2}, \\ E[\phi_3] &= \frac{2}{3} - \frac{2}{3}(1+H)^{3/2}. \end{aligned} \quad (2.3)$$

As H increases through 1, ϕ_1 merges with ϕ_2 and disappears, leaving ϕ_3 as the only static solution for $H > 1$. For $H < 0$ the story is the same, with ϕ and H negated throughout, so the physically-relevant solutions are $\tilde{\phi}_i(x) := -\phi_i(x)$, $i = 1 \dots 3$.

3 Numerical results

We took initial conditions corresponding to an antikink at $x_0 = -10$ travelling towards the boundary with velocity $v_i > 0$. (We found the setup with an incident antikink easier to visualise, but our results apply equally to kink-boundary collisions on negating ϕ and H .) Thus the initial profile was $\phi(x, 0) = \phi_1(x) - \tanh(\gamma(x - x_0)) + 1$ for $H > 0$ and $\phi(x, 0) = \tilde{\phi}_3(x) - \tanh(\gamma(x - x_0)) + 1$ for $H < 0$, where $\gamma = 1/\sqrt{1 - v_i^2}$. Our real interest was in the problem with the initial antikink infinitely far from the boundary, but the rapid decay of the antikink-boundary force (4.1), calculated below, meant that error in taking $x_0 = -10$ was small.

To solve the system numerically, we restricted it to an interval of length L , with the Neumann boundary condition imposed at $x = 0$ and a Dirichlet condition at $x = -L$. (Since we took run times such that radiation did not have time to reflect from the extra boundary and return, the boundary condition at $x = -L$ was anyway irrelevant.) We used a 4th order finite-difference method, explained in more detail in appendix A, on a grid of $N = 1024$ nodes with $L = 100$, so the spatial step was $\delta x \approx 0.1$, and a 6th-order symplectic integrator for the time stepping function, with time step $\delta t = 0.04$. Selected runs were repeated with other values of x_0 , L , N and δt to check the stability of our results.

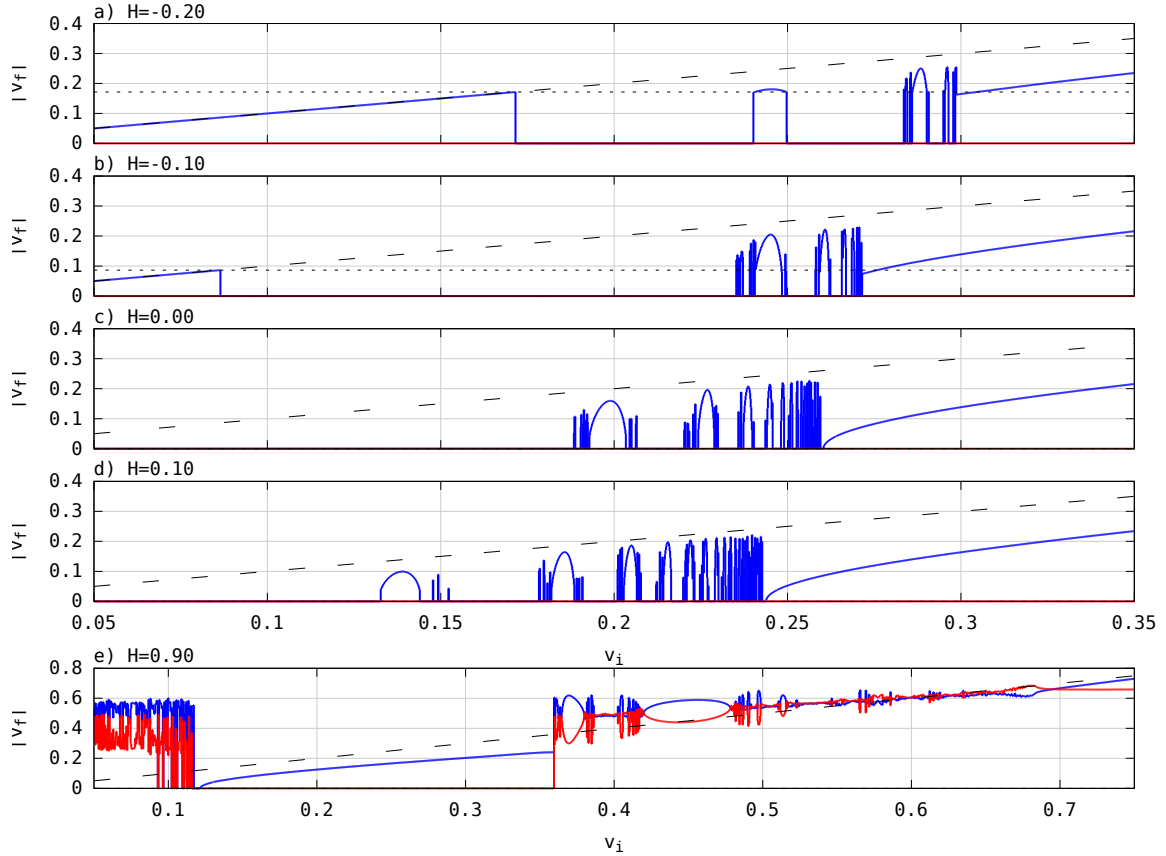


Figure 2. Final antikink velocities as functions of initial velocities. The dashed line indicates the result for a purely elastic collision. In the fifth plot, a kink can also be produced: its velocity is shown in red. The horizontal dotted lines in plots a and b show the relevant values of $v_{cr}(H)$, as given by equation (4.2) below.

Our simulations revealed a rich picture, aspects of which are summarised in figures 2 and 3. For all (H, v_i) pairs with $H < H_c \approx 0.6$, the antikink either reflects off the boundary with some velocity v_f , or becomes stuck to it – corresponding to $v_f = 0$ – to form a ‘boundary oscillon’. This latter configuration oscillates with a large (of order one) amplitude, and a below-bulk-threshold basic frequency. Just like the bulk oscillon (which it becomes in the limit $H \rightarrow 0$), it then decays very slowly into radiation. At $H = 0$ (figure 2c) the plot of $|v_f|$ as a function of v_i reproduces the well-known structure of resonant scattering windows in $K\bar{K}$ collisions on a full line [10–12]. For *negative* values of H (figures 2a and b) new features emerge. For v_i small, the antikink is reflected elastically from the boundary with very little radiation. As v_i increases above an H -dependent critical value v_{cr} , the antikink is trapped by the boundary, leaving only radiation in the final state. Increasing v_i further, scattering windows begin to open, until v_i exceeds an upper critical value and the antikink again always escapes. If the antikink does escape, its speed $|v_f|$ is always larger than some minimal value very slightly lower than v_{cr} , so (in contrast to the full-line situation) v_f is a discontinuous function of v_i , giving the windows the sharp edges mentioned in the intro-

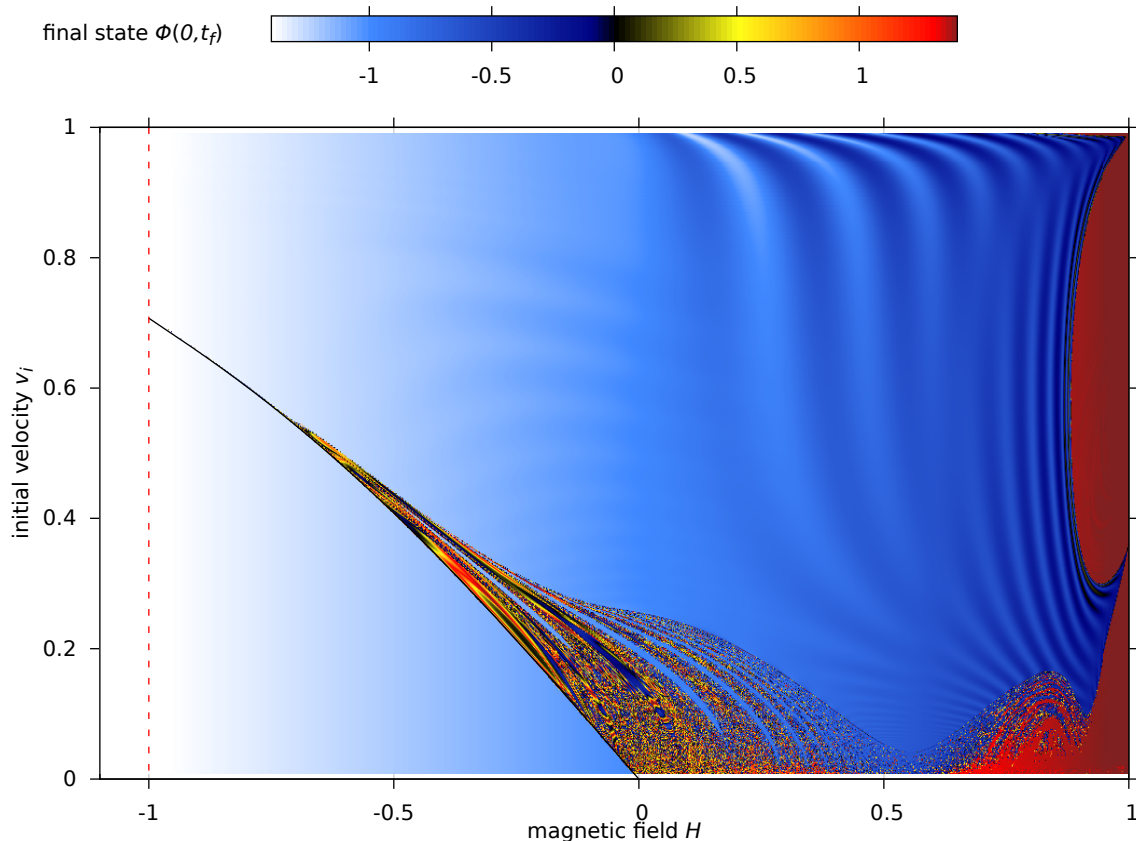


Figure 3. A ‘phase diagram’ of antikink-boundary collisions. The plot shows the value of the field at $x = 0$ a time $t_f = |x_0|/v_i + 100$ after the start of the simulation, as function of the boundary magnetic field H and the initial velocity v_i .

duction. For small *positive* values of H (figure 2d), v_f is instead a continuous function of v_i , the sequence of windows for $H = 0$ shifting towards lower velocities while preserving its general structure. Finally, for $H > H_c$ (figure 2e) other new phenomena arise which have no counterparts in the full-line theory; these will be discussed further in later sections.

4 Kink-boundary forces and the location of the low-velocity window

To understand the novel window of near-elastic scattering at low initial velocities when H is negative, seen in figures 2a and 2b, we start by evaluating the static force between a single antikink and the boundary. Placing the antikink at $x = x_0 < 0$, we add a possibly-singular ‘image’ kink at $x_1 > 0$ in such a way that the combined configuration satisfies the boundary condition at $x = 0$. From the standard full-line result, the force on the antikink from the image kink is equal to $32e^{-2(x_1-x_0)}$, or minus this if the image kink is singular. For $|H| \ll 1$ and $|x_0| \gg 1$ we find that the boundary condition requires $e^{-2x_1} = \frac{1}{4}H + e^{2x_0}$, so

$$F = 32 \left(\frac{1}{4}H + e^{2x_0} \right) e^{2x_0}. \quad (4.1)$$

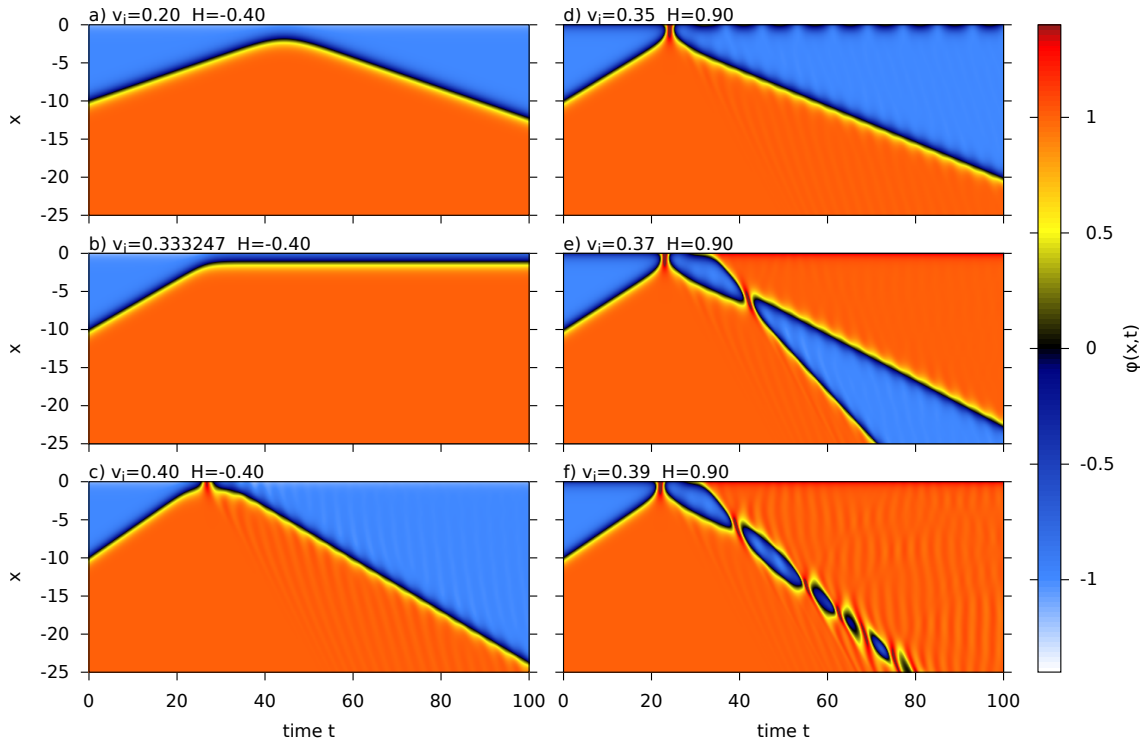


Figure 4. Example collisions for $H = -0.4$ (left column) and $H = 0.9$ (right column), illustrating various scattering scenarios. At negative H : (a) elastic recoil for low impact velocity; (b) saddle point production at the critical velocity, the antikink finishing on the top of the potential barrier; (c) single bounce with the antikink escaping back over the barrier. At positive H : (d) single bounce with the excitation of the $H > 0$ boundary mode; (e) kink production via collision-induced boundary decay; (f) bulk oscillon production. See also movies M01 – M07 and M11 of appendix B.

For $H < 0$ the force is repulsive far from the boundary, only becoming attractive nearer in. When $x_0 = \frac{1}{2} \log(-\frac{1}{4}H)$, $x_1 = \infty$ and the force vanishes, the antikink-kink configuration reducing to the unstable static solution $\tilde{\phi}_2$.

Now consider, again for $H < 0$, an antikink moving towards the boundary. If its velocity v_i is small, then it won't have sufficient energy to overcome the initially-repulsive force, and it will be reflected without ever coming close to $x = 0$, and without significantly exciting any other modes; this behaviour is illustrated in figure 4a. Increasing v_i , at some critical value v_{cr} the energy will be just enough reach the top of the potential barrier and create the static saddle-point configuration $\tilde{\phi}_2$, as shown in figure 4b. The value of v_{cr} can be deduced on energetic grounds: the initial energy is $\frac{4}{3}(1 - v_{cr}^2)^{-1/2} + E[\tilde{\phi}_3]$, while the final energy is $E[\tilde{\phi}_2] = \frac{2}{3} + \frac{2}{3}(1+H)^{3/2}$. Equating the two,

$$v_{cr}(H) = \sqrt{1 - 4((1+H)^{3/2} + (1-H)^{3/2})^{-2}}. \quad (4.2)$$

If v_i is just larger than v_{cr} , the antikink can overcome the potential barrier and approach the boundary; energy is then lost to other modes and so it is unable to return, and is trapped at

the boundary. Thus $v_{cr}(H)$ marks the upper limit of the windows of almost-perfectly-elastic scattering seen in figures 2a and 2b, and the lower edge of the ‘fractal tongue’ occupying the left half of figure 3. The curve $v_i = v_{cr}(H)$ is included in figure 3; it matches our numerical results remarkably well. Indeed, it can be seen from figure 7 below that the maximum error is of the order of 0.5%, which is rather small given that radiation was ignored in the derivation. Similar arguments show that, within this approximation, v_{cr} is the smallest possible speed for *any* escaping antikink, explaining the sharp (discontinuous) edges of all windows when $H < 0$.

5 The boundary mode

Next we consider the perturbative sector of the model, that is solutions of the form $\phi(x, t) = \phi_s(x) + \eta(x, t)$ where $\phi_s(x)$ is a static solution to the equations of motion and $\eta(x, t)$ is small. The full-line theory has a continuum of small linear perturbations about each vacuum with mass $m = 2$, while a static kink $\phi_K(x) = \tanh(x - X_0)$ has two discrete normalizable modes – the translational mode, and a vibrational mode with frequency $\omega_1 = \sqrt{3}$ – and a continuum of above-threshold states $\eta(x, t) = e^{i\omega t} \eta_k(x)$ where $\omega^2 = 4 + k^2$ and [19]

$$\eta_k(x) = e^{-ik(x-X_0)} (-1 - k^2 + 3ik \tanh(x - X_0) + 3 \tanh^2(x - X_0)). \quad (5.1)$$

Turning now to the half-line theory, we can regard $\phi_K(x)$ instead as the static half-line solution $\phi_1(x)$ to the boundary theory with $0 < H < 1$ and $\phi(-\infty) = -1$. Its linear perturbations must now satisfy $\partial_x \eta(x) = 0$ at $x = 0$. Setting $k = i\kappa$ this yields

$$\kappa^3 - 3\phi_0 \kappa^2 + (6\phi_0^2 - 4)\kappa - 6\phi_0^3 + 6\phi_0 = 0 \quad (5.2)$$

where $\phi_0 = \phi_1(0) = -\sqrt{1-H}$ and the frequency ω_B of the corresponding boundary mode satisfies $\omega_B^2 = 4 - \kappa^2$. The solutions of (5.2) for both negative and positive values of ϕ_0 are shown on the left-hand plot of figure 5; note that only solutions with $\kappa > 0$ can give rise to localised modes, and of these, κ must be less than 2 for ω_B to be real and the mode stable. We will denote the corresponding normalised profile function as $\eta_B(x) := \eta_{i\kappa}(x)/\eta_{i\kappa}(0)$, where $\eta_{i\kappa}(x)$ is given by (5.1) with $k = i\kappa$.

For $0 < H < 1$, we have $-1 < \phi_0 < 0$ and (5.2) has just one positive solution κ , which satisfies $\kappa < 2$: this is the single vibrational mode, localised near to the boundary. The linear perturbations of $\phi_2(x)$, the saddle-point solution, are also described by (5.2), but now with $\phi_0 = \phi_2(0) = +\sqrt{1-H}$. For these cases (5.2) has two positive solutions but one is larger than 2: this is the unstable mode of $\phi_2(x)$. Finally, for $H < 0$, the continuation of (5.2) to $\phi_0 < -1$ governs the spectrum of fluctuations about $\tilde{\phi}_3(x)$, the $H < 0$ vacuum in the $\phi(-\infty) = -1$ sector. There are no positive solutions in this regime and hence no vibrational modes of the boundary for $H < 0$. The right-hand plot of figure 5 summarises the situation, plotting the images of the positive- κ parts of the curves shown on the left under the mapping $(\phi_0, \kappa) \rightarrow (H, \omega_B^2) = (1 - \phi_0^2, 4 - \kappa^2)$. The grey dashed parts of the curve visible for $H < 0$ are included for completeness but do not describe vibrational modes of physical solutions – they correspond to ‘perturbations’ of the singular solution $\tilde{\phi}_4(x)$.

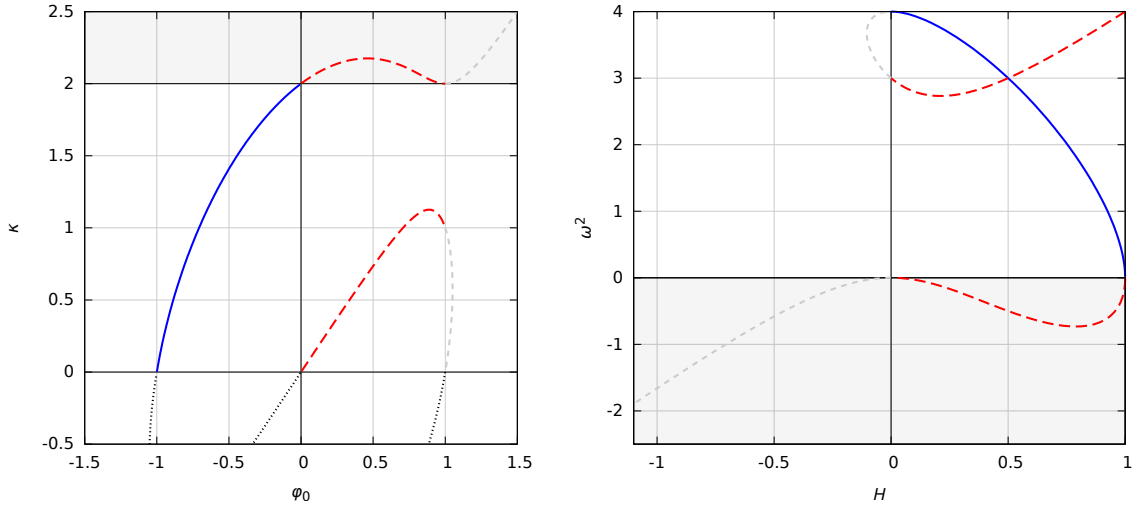


Figure 5. Linearised boundary mode analysis: on the left, the solutions of equation (5.2) as a function of $\phi_0 = \phi(0)$; on the right, the frequencies of localised boundary modes as a function of H .

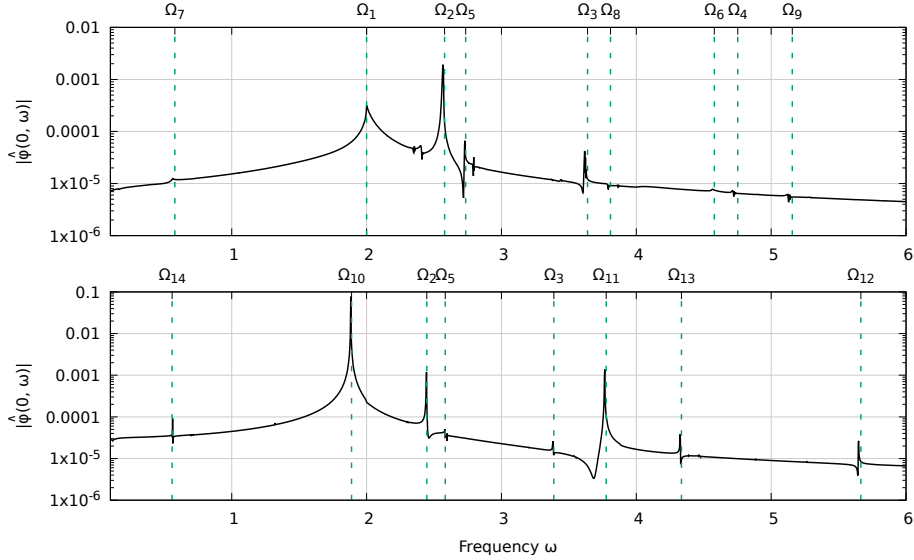


Figure 6. Power spectra at the boundary after a collision with $v_i = 0.5$, for $H = -0.1$ (upper) and $H = 0.3$ (lower).

These findings are confirmed by our numerical results. Figure 6 shows the Fourier transforms of $\phi(0, t)$ for $30 < t < 3030$, for antikink-boundary collisions with initial velocity $v_i = 0.5$, and $H = -0.1$ and 0.3 . The final velocity v_f of the reflected antikink is -0.382596 for $H = -0.1$ and -0.454014 for $H = 0.3$, so in both cases translational energy is lost to other modes during the collision.

For $H = -0.1$, the boundary does not have an internal mode, and only radiative modes with frequencies near to 2, the mass threshold, remain near to the boundary. The internal mode of the reflected antikink has frequency ω_1 , but this mode cannot be observed at the boundary since it is exponentially suppressed there. However nonlinear couplings

with other excitations create waves with frequencies at above-threshold multiples of ω_1 [20], which can propagate back to the boundary. The upper plot of figure 6 shows peaks at $\Omega_1 = 2$ and $\Omega_2 = \Omega(2\omega_1)$, where $\Omega(\omega) = \gamma(\omega + k(\omega)v_f)$ is the Doppler-shifted frequency of radiation emitted from the moving kink measured on the boundary. Higher harmonics at $\Omega_3 = \Omega(3\omega_1)$ and $\Omega_4 = \Omega(4\omega_1)$ are also visible, along with combinations of the internal mode of the antikink and the lowest continuum mode such as $\Omega_5 = \Omega(2+\omega_1)$ and $\Omega_6 = 2+\Omega(2\omega_1)$.

Many of these modes are also present in the $H = 0.3$ spectrum shown in the lower plot of figure 6, albeit at shifted locations because of the different final antikink velocity. However the plot is dominated by the internal boundary mode with frequency $\Omega_{10} = \omega_B = 1.888459$. The higher harmonics $\Omega_{11} = 2\omega_B$ and $\Omega_{12} = 3\omega_B$ are also visible, while interactions between radiation from the outgoing antikink and the boundary mode lead to peaks at $\Omega_{13} = \omega_B + \Omega(2\omega_1)$ and $\Omega_{14} = \omega_B - \Omega(2\omega_1)$.

6 The resonance mechanism in boundary scattering

For small nonzero values of $|H|$, the resonant energy exchange mechanism governing scattering in the bulk ϕ^4 model is changed in two ways in the boundary theory: (i) the attractive force acting on the antikink near to the boundary is modified, in particular becoming repulsive at greater distances when H is negative; (ii) after the initial impact, energy can be stored not only in the internal mode of the antikink, but also, for positive values of H , in the boundary mode. These factors change the resonance condition for energy to be returned to the translational mode of the antikink on a subsequent impact after some integer number of oscillations of the antikink’s internal mode, shifting (and, for negative H , sharpening) the windows seen in figures 2 a-d. This return can happen after two, three or more bounces from the boundary, leading to a hierarchy of multibounce windows as in the full-line situation. Our numerical results suggest that for small positive values of H the contribution of the boundary mode in the resonant energy transfer is not significant.

For larger values of $|H|$ other new features appear. For $H < 0$ the first is the resurrection of a two-bounce window that was observed to be missing from the full-line scattering process by Campbell et al in [10]. Figure 2a includes a scattering window centred at $v_i \approx 0.245$ which is *not* the continuation of any of the windows seen in figures 2 b-d; the same window can be seen in figure 3 running from $(H, v_i) = (-0.135, 0.202)$ to $(H, v_i) = (-0.489, 0.417)$, and the top plot of figure 7, running from $(H, v_i - v_{cr}) = (-0.135, 0.084)$ to $(H, v_i) = (-0.489, 0.023)$. The emergence of this window as H decreases below $H \approx -0.136$ is shown in more detail in the left-hand set of plots of figure 8. The nature of the new window is made clear by the plots in figure 9, which shows $\phi(0, t)$ for v_i inside the first three two-bounce windows for $H = -0.2$, and also for $H = 0$, which is equivalent to the full-line case. The ‘wobbles’ between the large dips in such plots count the oscillations of the internal antikink mode between bounces [10]. As can be seen from the figure, the minimum number of oscillations supporting antikink escape is one smaller for $H = -0.2$ than it was for $H = 0$, giving rise to the extra window. A complementary process of ‘window destruction’ occurring for $H > 0$ can be seen on a close examination of figure 3, and on the right-hand set of plots of figure 8. Decreasing H further, we also observed interesting structures at the

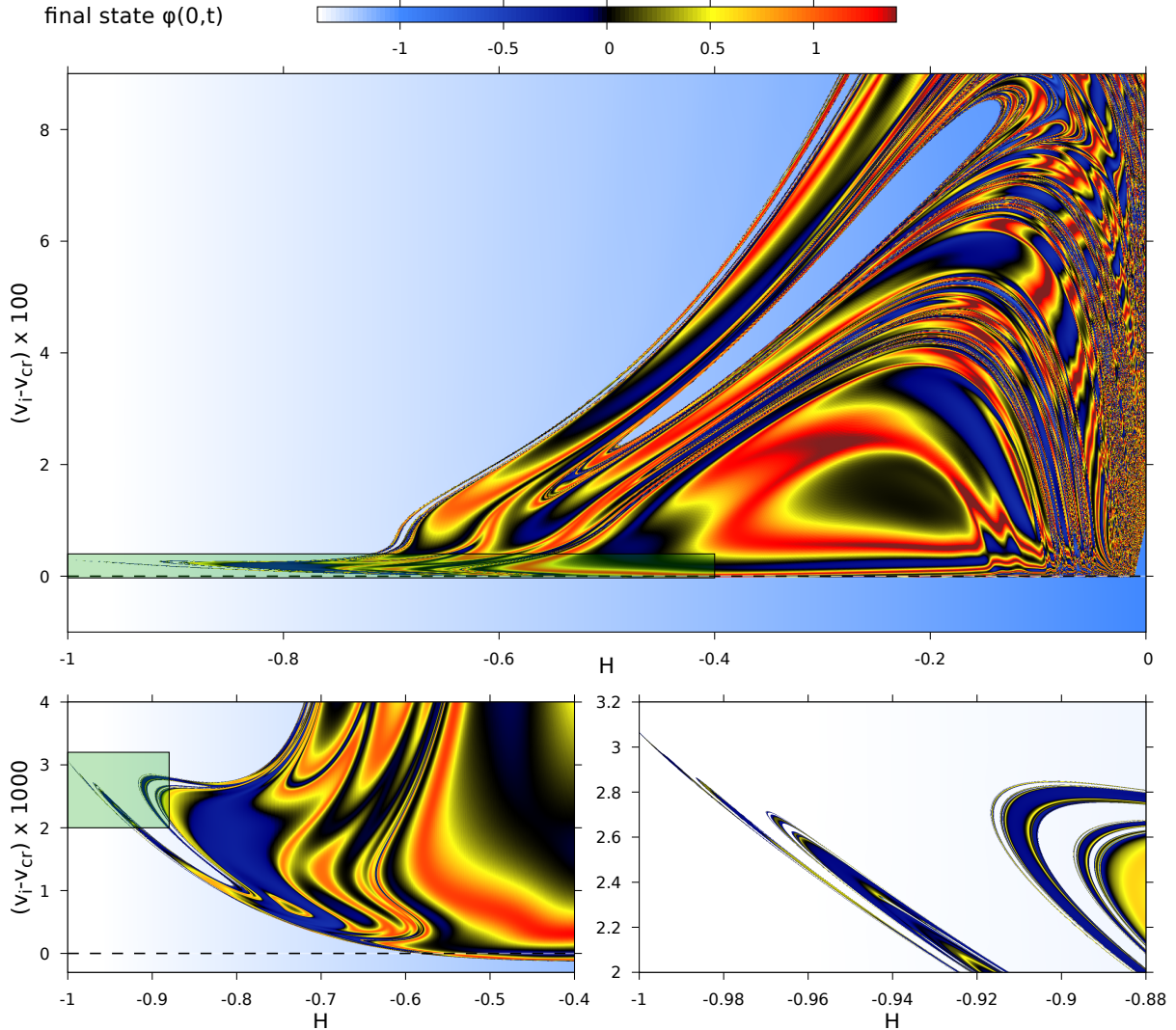


Figure 7. Zoomed-in views of the region near the tip of the fractal tongue of figure 3. Note that the vertical axes show multiples of $v_i - v_{cr}$, where $v_{cr} = v_{cr}(H)$ is the theoretical upper limit of the near-elastic scattering window given by the formula (4.2).

tip of the fractal tongue, near to $H = -1$, with resonance windows merging to give rise to a pattern of half-rings on the phase diagram. These are shown in the lower two plots in figure 7.

For $H > 0$, the scattering can induce the metastable ϕ_1 boundary to decay to ϕ_3 , the true ground state, with the creation of an extra kink. This process, which has no analogue in the full-line theory, is visible in the extra red ‘kink’ line in figure 2e. The principal region of boundary decay occupies the solid red area on the right edge of figure 3, and is examined in more detail in figure 10. If the boundary mode is sufficiently strongly excited by the initial antikink impact, it behaves as an intermediate state prior to the escape of a kink from the boundary, analogous to the intermediate oscillon state in the process of $K\bar{K}$ pair production on the full line [18, 20, 21]. Depending on their relative velocities, the reflected antikink and the subsequently-emitted kink may appear separately in the final

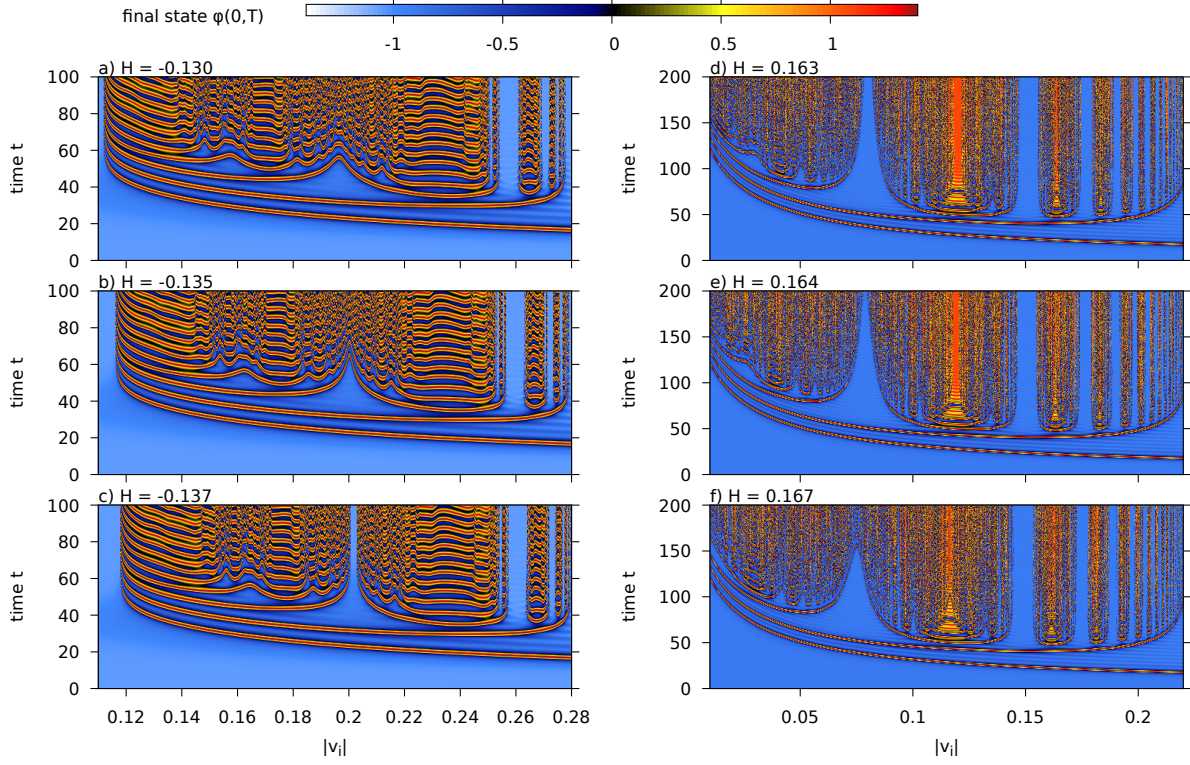


Figure 8. Scans of $\phi(0,t)$ for various values of H , showing the emergence (on the left) and destruction (on the right) of a two-bounce window as H moves away from zero.

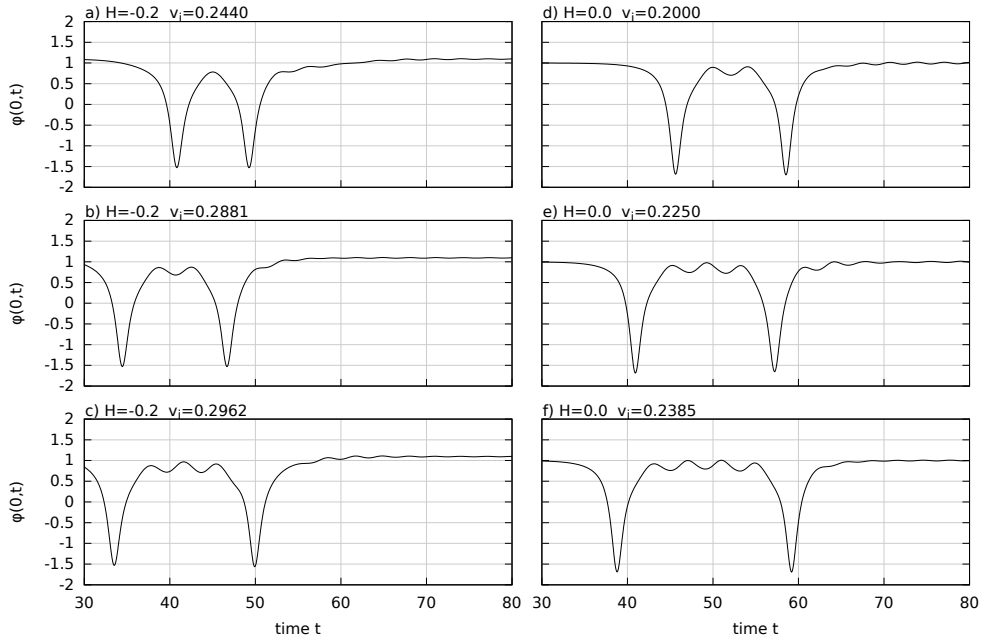


Figure 9. Plots of $\phi(0,t)$ for v_i inside the first three two-bounce windows for $H = -0.2$ (left) and for $H = 0$ (right).

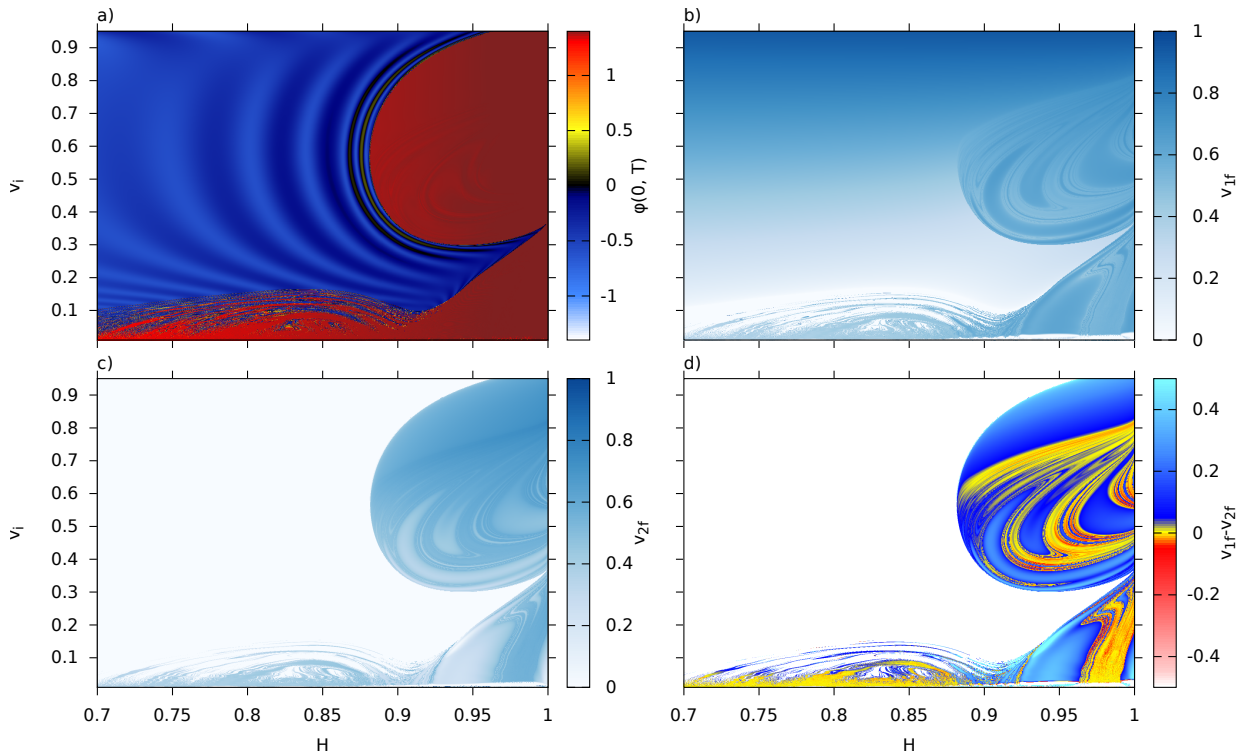


Figure 10. Antikink-boundary scattering at large H . (a): a zoomed-in view of figure 3 showing the value of the field at $x = 0$ a time $t_f = |x_0|/v_i + 100$ after the start of the simulation; (b): the measured final velocity of the reflected antikink; (c): the measured final velocity of the emitted kink, if present, white being plotted otherwise; (d): the difference between these two velocities.

state, or recombine to form a bulk oscillon. Such collisions lead themselves to a fractal-like structure with windows where the antikink and kink separate interspersed with regions of oscillon production, just as in the full-line theory (though with added complications due to interference with radiation from the boundary). Some of this structure can be seen in figure 10d, where the blue regions inside the zone of boundary decay show windows of antikink and kink separation, while the yellow regions correspond to the production of a bulk oscillon, and also in the movies M11 and M12. Spacetime plots of some of the relevant processes, for $H = 0.90$, are shown in the right panels of figure 4: scattering of the antikink with excitation of the boundary mode, but no kink production (d); production of a separated $K\bar{K}$ pair, with the boundary decaying to the true ground state (e); and recombination of the $K\bar{K}$ pair to form a bulk oscillon (f). A further intriguing feature of the region of boundary decay, clearly visible in figures 3 and 10, is the cusp-like nick, terminating at $(H, v_i) \approx (1, 0.365)$, which splits it into two disconnected parts. This appears to be associated with a velocity-dependent vanishing of the effective coupling between the incident antikink and the boundary mode. It would be very interesting to find an analytical understanding of this phenomenon, but we will leave this for future work.

7 Radiative decay of the boundary mode

A significant feature of the ϕ^4 model is that its spectrum of perturbative oscillations around the static kink or antikink solutions contains an internal vibrational mode. If the amplitude of the excitation is small enough and nonlinear corrections can be neglected, this mode oscillates with almost-constant amplitude A and frequency $\omega_d = \sqrt{3}$. For larger amplitudes nonlinearities start to play an important role. It has been shown [20] that the first anharmonic correction to the internal mode oscillation results in the appearance of an outgoing wave with frequency $2\omega_d$, which is above the mass threshold. The corresponding rate of radiative energy loss is $dE/dt \sim A^4$, causing the mode to decay. The resulting time dependence of the amplitude of the internal mode follows the law $dA/dt \sim A^3$, where the explicit value of the proportionality constant can be found using a Green's function technique [20].

For our boundary theory, we have observed a similar pattern in the decay of small-amplitude excitations of the boundary mode, but with a number of interesting new features. For small positive values of H , the frequency ω_B of the linearised boundary mode, as predicted by (5.2), satisfies $2\omega_B > 2$, and so the second harmonic of this mode is able to propagate in the bulk¹. But as the boundary magnetic field H increases, the frequency of the boundary mode decreases, and when $H > H_2 \approx 0.925$, $2\omega_B$ dips below 2 and the situation changes. The second harmonic can no longer propagate into the bulk, and this channel of radiative energy loss from the boundary is terminated. Only the next harmonic, which appears in the third order of the perturbation series, can be seen in the power spectrum. The radiation loss rate becomes $dE/dt \sim A^6$ and the decay rate is reduced to $dA/dt \sim A^5$.

The situation changes again as H increases beyond $H = H_3 \approx 0.982$, when $3\omega_B$ falls below 2 and the third harmonic joins the second, trapped below the mass threshold. Theoretically, as $H \rightarrow 1$ and $\omega_B \rightarrow 0$ this pattern will repeat an infinite number of times, so that whenever $\frac{2}{n+1} < \omega_B < \frac{2}{n}$, the amplitude of the decaying mode should satisfy, to leading order, the equation $dA/dt \sim A^{2n-1}$.

Figure 11 shows the behaviour of the field on the boundary and at $x = -50$, in the far field zone, with initial conditions $\phi(x, 0) = \phi_1(x) + 0.05 \eta_B(x)$, $\phi_t(x, 0) = 0$ and $H = 0.90 < H_2$. The power spectrum of the field on the boundary is dominated by boundary mode oscillating with the theoretically predicted frequency $\omega_B = 1.08509$. There are also two peaks at $2\omega_B$ and $3\omega_B$. Since $\omega_B < m$, this lowest mode cannot propagate and indeed, there is no trace of it in the far field zone. The mode with the frequency $2\omega_B$ is already in the scattering spectrum, so this mode does propagate, causing the energy loss from the boundary mode, as seen in figure 11a.

The picture is different when $H = 0.94 > H_2$ (see figure 12). The mode with frequency $\omega_B = 0.93643$ still dominates the power spectrum of the boundary excitations, but its decay is much slower, reflecting the fact that the mode $2\omega_B$ is now below the mass threshold and cannot propagate into the bulk. As can be seen from the power spectrum in the far field zone plotted in figure 12d, the radiation is much less than in the previous case. There are two dominant frequencies, $\omega = 2$ and $\omega = 3\omega_B$. The presence of the peak at $3\omega_B$ is natural, since this is the first harmonic above the mass threshold. The peak at $\omega = 2$ originates from

¹Recall that $m = 2$ is the mass threshold for the bulk theory.

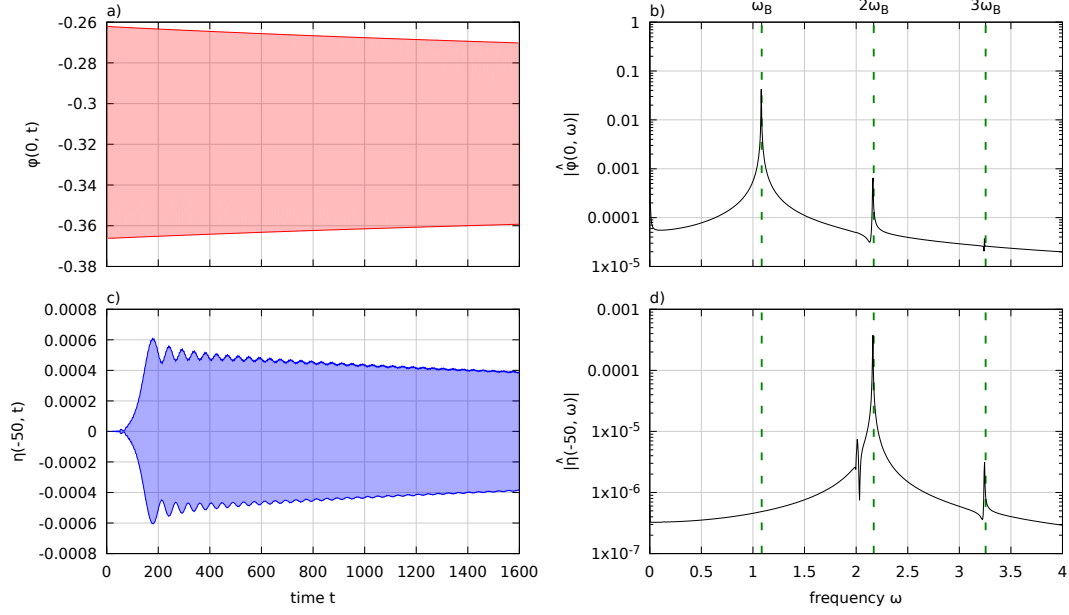


Figure 11. Evolution of the boundary mode for $H = 0.90 < H_2$, with initial conditions $\phi(x, 0) = \phi_1(x) + 0.05\eta_B(x)$, $\phi_t(x, 0) = 0$: a) the amplitude of the boundary mode as a function of time; b) its power spectrum, found by taking the Fourier transform of $\phi(0, t)$ for $0 < t < 1600$; c) the values of $\eta(x, t) := \phi(x, t) - \phi_1(x)$ at $x = -50$; d) its power spectrum, taken from $\eta(-50, t)$ for $200 < t < 1600$. In plots a) and c), solid non-transparent lines join local extrema of the measured field at the given position.

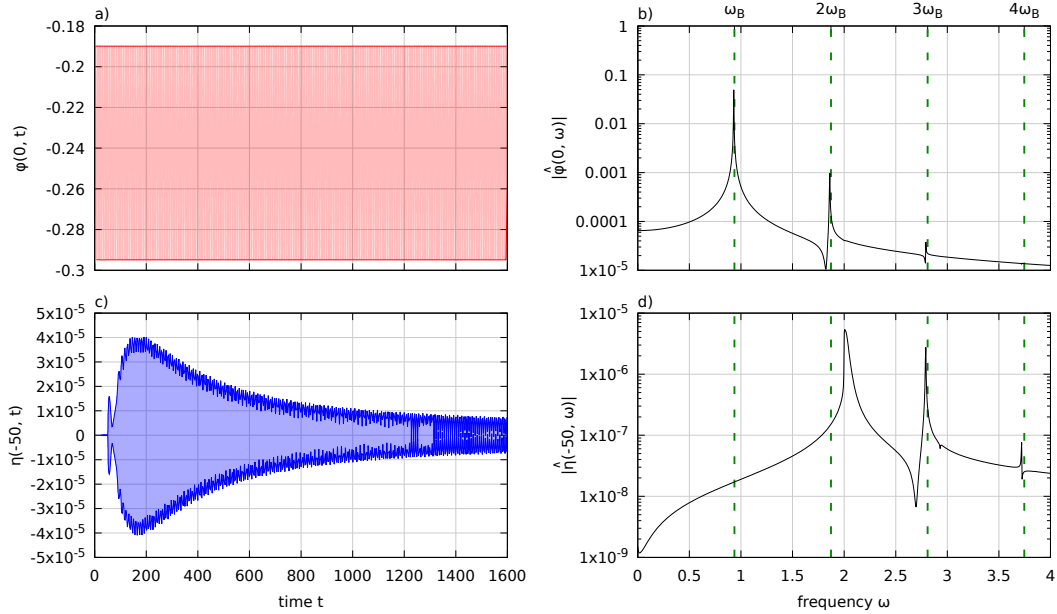


Figure 12. The same sequence of plots as in figure 11, but now for $H = 0.94 > H_2$.

near-threshold bulk modes, excited by the initial conditions via the nonlinearities, which disperse only slowly away from the boundary [22].

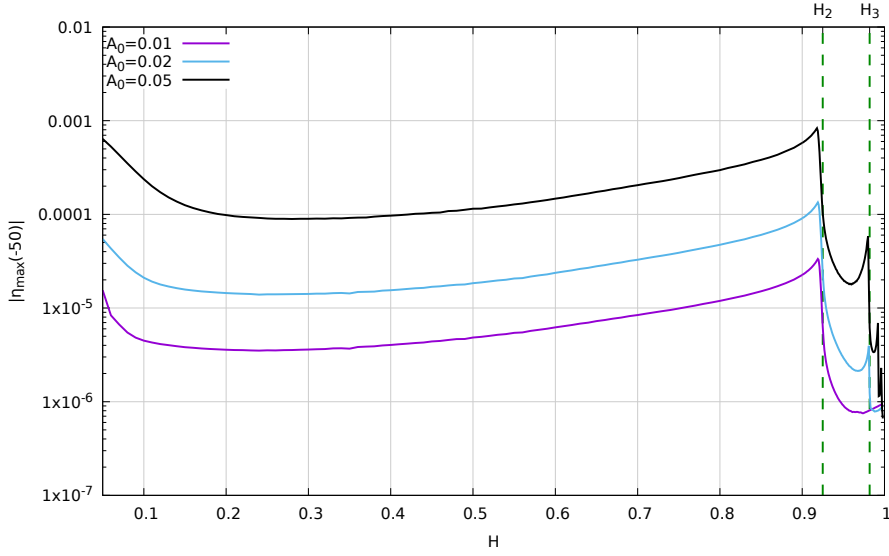


Figure 13. Maximal radiation amplitude $|\eta_{\max}(x)|$, where $\eta(x, t) = \phi(x, t) - \phi_1(x)$ is the deviation of the field from its static value, at $x = -50$ for the kicked initial conditions $\phi(x, 0) = \phi_1(x)$, $\phi_t(x, 0) = A_0 \omega_B \eta_B(x)$ as a function of H , for three different values of A_0 .

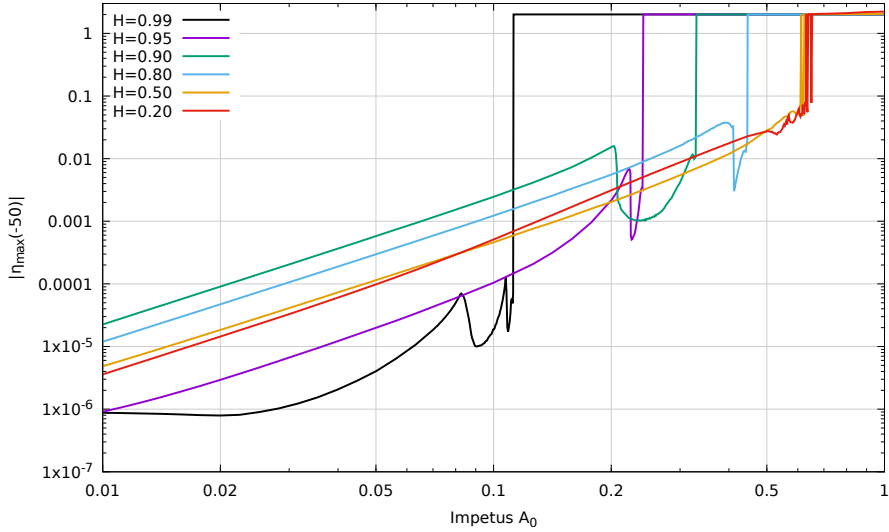


Figure 14. A log-log plot of the maximal radiation amplitude at $x = -50$ for the kicked initial conditions $\phi(x, 0) = \phi_1(x)$, $\phi_t(x, 0) = A_0 \omega_B \eta_B(x)$ as a function of A_0 . Note that for small A_0 and $H < H_2$ the power law decay rate is universal.

Another test of the scenario is to consider the radiation from a “kicked” boundary initial condition $\phi(x, 0) = \phi_1(x)$, $\phi_t(x, 0) = A_0 \omega_B \eta_B(x)$ in the far field zone. Our numerical results for this case are presented in figures 13 and 14.

Figure 13 shows the H -dependence of maximal amplitude of the field measured at $x = -50$, far away from the boundary, for three small values of the initial impetus A_0 given to the boundary mode. Note that the radiation amplitude drops sharply when H crosses

H_2 and H_3 , as predicted by our general considerations.

Figure 14 shows a log-log plot of the dependence of the maximal amplitude at $x = -50$ on A_0 . For small values of A_0 and $H < H_2$, all curves have the same slope, fitting the expected $\sim A_0^2$ dependence. The curve for $H = 0.95$ shows a significant reduction in the radiation amplitude, reflecting the loss of a decay channel as H passes H_2 . However its slope for small values of A_0 appears to be relatively unchanged from that of the previous curves, even though our previous considerations based on the propagation of the third harmonic would suggest an $\sim A_0^3$ dependence. It may be that slow (near-threshold) bulk modes, visible in figure 12d in the peak at $\omega = 2$, are obscuring the effect we are looking for. It is possible that this could be tested by waiting significantly longer before measuring the radiation, to allow the slow modes to die away, but a more-detailed study would be needed to draw a clear conclusion.

Another interesting feature visible on each curve is that as A_0 reaches some (curve-dependent) critical value, the radiation flux suddenly dips. As will be discussed in the next section, this effect is associated with the nonlinear effect of the reduction in the frequency of the boundary mode with increasing amplitude.

Finally, for even larger values of the initial impetus we can see a large increase of the amplitude of the field in the far zone. This is a signature of a non-perturbative effect, the excitation at the boundary becoming strong enough to destabilise it completely, with the emission of a kink into the bulk flipping the field there into the other vacuum. Some further observations concerning this phenomenon are reported in section 9 below.

8 Higher-order nonlinear effects and amplitude-dependent decay rates

In the last section we principally considered boundary mode decay in the small-amplitude regime where the boundary mode itself could be treated linearly. For larger amplitudes the frequency of the mode's oscillation is lowered, just as in the case of an anharmonic oscillator or the simple pendulum. Numerical simulations of the oscillations of a full-line kink [20] also exhibit this behaviour, which is typical for many nonlinear systems.

In the evaluation of the critical values H_n above, we implicitly assumed that the amplitude of the excitation was small, so that its frequency was that predicted by the linearised equations. However for larger amplitudes, given the amplitude-dependent frequency reduction just described, it is possible that even for $H < H_2$, the actual frequency of the boundary mode, $\tilde{\omega}_B$, will be lower than $m/2$. Then the decay rate will be slower than that observed for smaller amplitudes, since the second harmonic will not couple directly with any propagating bulk modes. However, the amplitude of the boundary mode will decrease with time due to the outgoing radiation, causing its frequency to grow. Provided $H < H_2$, once the amplitude has decreased far enough, the second harmonic will enter the scattering spectrum. In such a case we can expect to observe an intriguing phenomenon: while initially the radiation flux from the boundary is relatively small and the decay rate rather slow, after some time there will be a sudden increase of the radiation flux and a switch to a much faster decay rate.

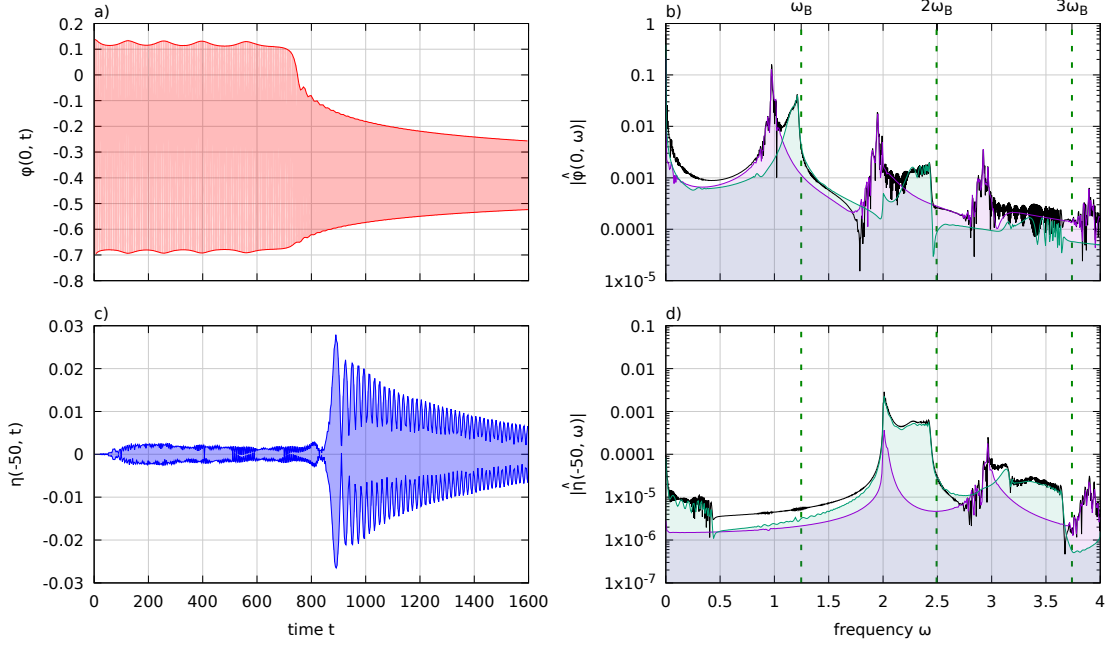


Figure 15. Evolution of the boundary mode for $H = 0.8393 < H_2$ and large initial amplitude $A_0 = 0.3$. Plots a) and c) show the time evolution of the amplitudes of the boundary mode and radiation field respectively, from the values of the field at $x = 0$ and $x = -50$. Plots b) and d) show power spectra at the positions $x = 0$ and $x = -50$. The black lines show the power spectra from $\dot{\phi}(0, t)$ for times $0 < t < 1600$ (plot b)) and $\dot{\phi}(-50, t)$ for times $200 < t < 1600$ (plot d)). The purple and green lines and filled areas show the power spectra for times before and after the transition ($0 < t < 750$ and $750 < t < 1600$ for $x = 0$; $200 < t < 800$ and $800 < t < 1600$ for $x = -50$).

Numerical work confirms that this effect really exists, as can be seen in figure 15 and movie M13, which show the decay of the amplitude of the boundary mode. For about the first 750 units of time the amplitude changes very slowly, albeit with a small modulation, after which there is a sudden transition to a much more rapid decay. In the far field zone this effect can be observed as a sudden jump of the radiation flux, by about one order of magnitude.

In the power spectrum plotted in figure 15d one can clearly see a large peak just below $\omega = 1$, which is the initial frequency of the mode. While the amplitude slowly decreases the frequency grows until it crosses 1, after which point the decay runs much faster. We can also see a drift of the frequency up to $\omega_B = 1.24666$.

This slow-then-fast behaviour is reminiscent of higher-dimensional oscillon decay. In [23–25] it was observed that oscillons in two and three spatial dimensions lose their energy very slowly for tens of thousands of oscillations until they reach some critical frequency, above which they quickly decay to the vacuum.

9 Creation of kinks from an excited boundary

The final phenomenon we investigated was the creation of kinks from the metastable boundary. We previously observed that this could be induced in certain scattering processes at large H . To view it in isolation, we instead excited the boundary mode directly, taking initial conditions of the two types (“stretched” and “kicked”) used earlier. First, we used initial condition

$$\phi(x, 0) = \phi_1(x) + A_0 \eta_B(x), \quad \phi_t(x, 0) = 0 \quad (9.1)$$

with $\eta_B(x)$ the boundary profile for the linearised problem, as an approximation to the boundary mode at its largest deviation from equilibrium; and second, we took

$$\phi(x, 0) = \phi_1(x), \quad \phi_t(x, 0) = A_0 \omega_B \eta_B(x) \quad (9.2)$$

representing the “kicked” boundary. As before, we normalized the profile of the boundary mode in such a way that $\eta_B(0) = 1$.

In both cases, if A_0 is taken to be sufficiently small, the boundary oscillates with frequency ω_B and the amplitude A_0 . However, as A_0 becomes larger, the nonlinear processes discussed above start to play a significant role and further, as the initial energy of the excited mode becomes sufficient, outgoing kinks can be observed in the far zone, as seen in figures 16 and 17.

Note that for large $H \rightarrow 1$ the boundary mode profile resembles the difference between the unstable boundary solution (a saddle point of the energy) and the stable boundary solution:

$$\eta_B(x) \approx \frac{\tanh(x + X_0) - \tanh(x - X_0)}{2 \tanh(X_0)} \quad (9.3)$$

Therefore the boundary mode, with appropriate amplitude, being added to the static boundary solution yields the unstable boundary. When the solution crosses the saddle point of energy it decays into another static solution with an additional kink is emitted from the boundary.

Therefore the critical value of the amplitude of the boundary mode for the production of the kinks is:

$$A_{crit} = \phi_2 - \phi_1 = 2\sqrt{1 - H}. \quad (9.4)$$

This critical amplitude is in very good agreement with the first type of the initial conditions for positive values of A_0 . Only for very small values of A_0 is there a symmetry $A_0 \rightarrow -A_0$. For larger $A_0 > 0$ the excitation have less energy than the excitation for $-A_0$. Therefore the critical line for kink creation, from the left side of the plot, is much closer to the centre ($A_0 = 0$).

For initial conditions of the second type, the energy for A_0 and $-A_0$ is exactly the same and therefore the plots look much more symmetric. For $H \rightarrow 1$ the critical amplitude is almost exactly $A_{crit} = \sqrt{1 - H}$, half as big as in the first case.

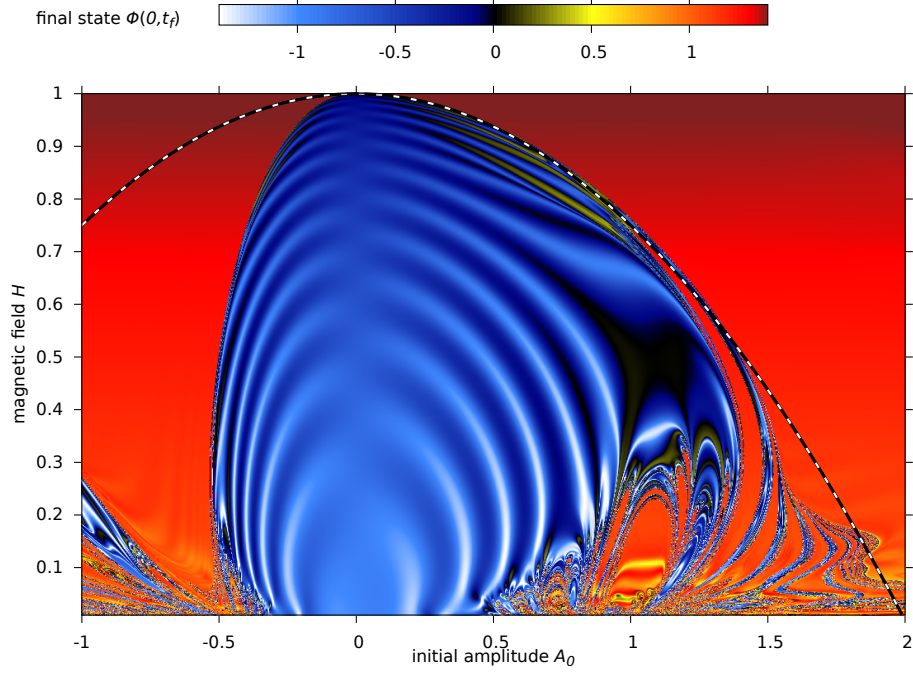


Figure 16. The field value on the boundary at time $t_f = 50$ for initial conditions $\phi(x, 0) = \phi_B(x) + A_0\eta_B(x)$, $\phi_t(x, 0) = 0$. The blue colour represents the region without kink creation. The dashed line corresponds to the function $H = 1 - A^2/4$.

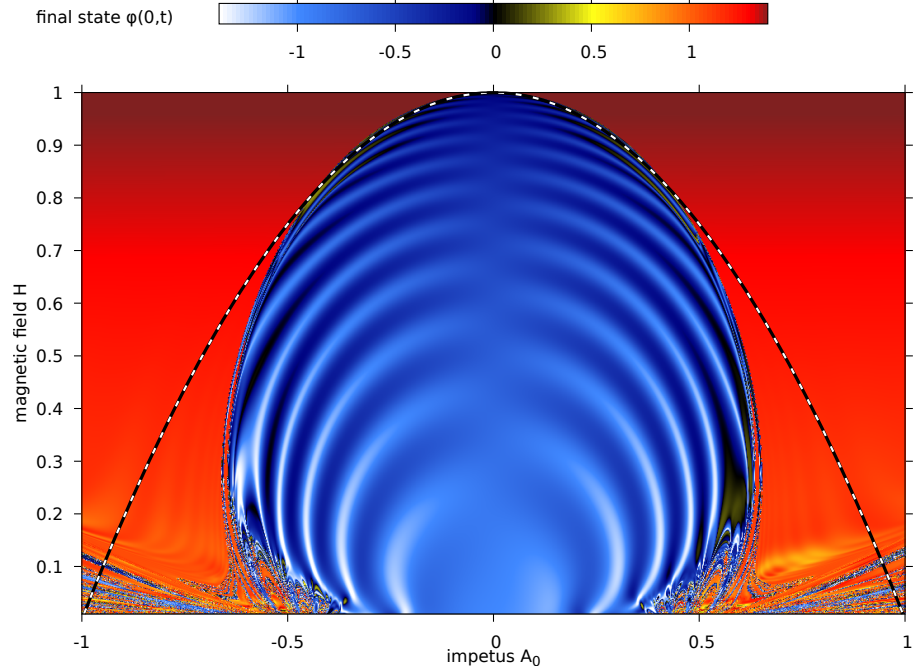


Figure 17. The field value on the boundary at time $t_f = 50$ for initial conditions $\phi(x, 0) = \phi_B(x)$, $\phi_t(x, 0) = A_0\omega_B\eta_B(x)$. The blue colour represents the region without kink creation. The dashed line corresponds to the function $H = 1 - A^2$.

10 Conclusions

Our investigations of the boundary ϕ^4 theory have shown that it offers a considerably richer variety of resonance phenomena than the bulk theory, within a setting where analytical progress can be made. Key features include the modification of the force leading to the sharpening of window boundaries and the new critical velocity v_{cr} , the resurrection of the first ‘missing’ scattering window, the observation of the boundary oscillon, and the collision-induced decay of the metastable boundary vacuum for H near to 1. Much of our work has been numerical and many issues remain for further study, the most pressing being the development of a reliable moduli space approximation incorporating the boundary degrees of freedom (see [9] for some earlier work on this issue). This model is sufficiently simple that it should offer the ideal playground for the development of better analytical techniques for the understanding of more general nonintegrable field theories.

Acknowledgements

We would like to thank Piotr Bizoń, Robert Parini and Wojtek Zakrzewski for discussions. The work of PED was supported by an STFC Consolidated Grant, ST/L000407/1, and by the GATIS Marie Curie FP7 network (gatis.desy.eu) under REA Grant Agreement No 317089. AH thanks the BSU Student Grant Program for support, and YS thanks the Russian Foundation for Basic Research (Grant No. 16-52 -12012), DFG (Grant LE 838/12-2) and JINR Bogoljubov-Infeld Programme.

A Numerical methods

In this Appendix we describe some details of the numerical methods used in our simulation. In our numerical code we used the following discretization:

$$u_n = \phi(-nh), \quad n = 0 \dots N. \quad (\text{A.1})$$

To calculate spatial derivatives we used a fourth-order central difference scheme

$$D^2 u_n = \frac{1}{12h^2} (-u_{n-2} + 16u_{n-1} - 30u_n + 16u_{n+1} - u_{n+2}) \quad (\text{A.2})$$

for all points far enough from the boundary, $n \leq 2$. This scheme can be derived using Lagrange polynomial approximation:

$$u(x) = \sum_{i=n-m}^{n+m} u_i \ell_i(x), \quad \ell_i(x) = \prod_{\substack{j=n-m \\ j \neq i}}^{n+m} \frac{x - jh}{ih - jh}. \quad (\text{A.3})$$

However for the two points closest to the boundary we have to use a different basis

$$u(x) = H\bar{\ell}_0(x) + \sum_{i=0}^3 u_i \tilde{\ell}_i(x), \quad (\text{A.4})$$

where

$$\tilde{\ell}_{i>0}(x) = \frac{x^2}{(ih)^2} \prod_{\substack{j=1 \\ j \neq i}}^3 \frac{x - jh}{ih - jh}, \quad (\text{A.5})$$

$$\tilde{\ell}_0(x) = \left(1 + \frac{11}{6}x\right) \prod_{j=1}^3 \frac{x - jh}{-jh}, \quad (\text{A.6})$$

$$\bar{\ell}_0(x) = x \prod_{j=1}^3 \frac{x - jh}{-jh}. \quad (\text{A.7})$$

Note that for points within the interpolation intervals

$$\ell_i(x_j) = \tilde{\ell}_i(x_j) = \delta_{ij}, \quad \bar{\ell}(x_i) = 0, \quad \tilde{\ell}'_i(0) = 0, \quad \bar{\ell}'(0) = 1. \quad (\text{A.8})$$

The above relations prove that formula (A.4) really interpolates the function with appropriate boundary condition

$$u(nh) = u_n, \quad n \leq 3 \quad \text{and} \quad u'(0) = H. \quad (\text{A.9})$$

From this approximation it is straightforward to calculate the second derivative for the first two points:

$$D^2u_0 = -\frac{1}{18h^2} (85u_0 + 66hH - 108u_1 + 27u_2 - 4u_3), \quad (\text{A.10})$$

$$D^2u_1 = \frac{1}{18h^2} (29u_0 + 6hH - 54u_1 - 2u_3 + 27u_2). \quad (\text{A.11})$$

B Supplementary material

We have prepared a number of short movies, labelled M01 ... M13, to illustrate aspects of our findings, which are listed in this appendix. The movies themselves can be found at [17].

The first six movies show the processes depicted in figure 4 a – f:

[M01_BndryScattering_Hminus040_v020.mov](#): $H = -0.4$, $v = 0.20 < v_{cr}(H)$

Almost-perfect reflection of the incident antikink, which has insufficient energy to get over the saddle-point potential barrier.

[M02_BndryScattering_Hminus040_v0333.mov](#): $H = -0.4$, $v = 0.333 = v_{cr}(H)$

Antikink incident at the critical velocity, leading to the creation of the saddle-point configuration. Note, this movie (and the associated figure 4b) is somewhat idealised, as in practice it is impossible to tune the initial velocity finely enough to hit the true critical velocity precisely. Instead, we patched together an animation up to $t = 40$ with the static solution thereafter.

[M03_BndryScattering_Hminus040_v040.mov](#): $H = -0.4$, $v = 0.40 > v_{cr}(H)$

Single bounce, with subsequent escape of the antikink. Note that the acceleration of the antikink after it surpasses the potential barrier is clearly visible.

[M04_BndryScattering_Hplus090_v035.mov](#): $H = 0.9$, $v = 0.35$

Single bounce, with excitation of both the $H > 0$ boundary mode and the internal mode of the antikink.

[M05_BndryScattering_Hplus090_v037.mov](#): $H = 0.9$, $v = 0.37$

Single bounce exciting the boundary mode strongly enough to induce decay of the metastable boundary state, creating an additional kink in the bulk.

[M06_BndryScattering_Hplus090_v039.mov](#): $H = 0.9$, $v = 0.39$

A similar process to M5, but here the relative velocities of the emitted kink and antikink are such that a bulk oscillon is formed instead of a separated kink-antikink pair.

The next six movies scan through a range of velocities at constant H . Movies M07 – M10 show ‘traditional’ window formation as in the full-line case (equivalent to M09). The sharpened edges of the windows for $H < 0$, caused by the presence there of a potential barrier, are visible on careful comparison of M7 and M8 (for $H < 0$) with M9 and M10 (for $H \geq 0$). For movies M11 and M12, H is in the region where collision-induced boundary decay is possible.

[M07_VelocityScan_Hminus040.mov](#): $H = -0.4$

[M08_VelocityScan_Hminus020.mov](#): $H = -0.2$

[M09_VelocityScan_H000.mov](#): $H = 0$

[M10_VelocityScan_Hplus020.mov](#): $H = 0.2$

[M11_VelocityScan_Hplus090.mov](#): $H = 0.9$

[M12_VelocityScan_Hplus095.mov](#): $H = 0.95$

Finally, movie M13 shows the slow-then-fast relaxation of the boundary mode. Four plots are shown: on the left, the field values next to, and slightly further from, the boundary; on the right, the amplitude of the field at the boundary, and an estimate $\omega(0, t) := 2\pi/T$ of its instantaneous frequency, where T is the time between successive minima of $\phi(0, t)$.

[M13_Relaxation_Hplus08393_A030.mov](#): $H = 0.8393$, $A_0 = 0.3$

References

- [1] P. Fendley, “Kinks in the Kondo problem”, *Phys. Rev. Lett.* **71** (1993) 2485
doi:10.1103/PhysRevLett.71.2485 [cond-mat/9304031].
- [2] O.H. Olsen and M.R. Samuelsen, “Fluxon propagation in long Josephson junctions with external magnetic field”, *J. Appl. Phys.* **52** (1981) 6247
doi:http://dx.doi.org/10.1063/1.328567.

- [3] F. Alcaraz, M. Barber, M. Batchelor, R. Baxter and G. Quispel, “Surface exponents of the quantum XXZ, Ashkin-Teller and Potts models”, *J. Phys. A* **20** (1987) 6397
doi:10.1088/0305-4470/20/18/038.
- [4] C.L. Kane and M.P.A. Fisher, “Transmission through barriers and resonant tunneling in an interacting one-dimensional electron gas”, *Phys. Rev. B* **46** (1992) 15233
doi:10.1103/PhysRevB.46.15233.
- [5] S. Ghoshal and A.B. Zamolodchikov, “Boundary S matrix and boundary state in two-dimensional integrable quantum field theory”, *Int. J. Mod. Phys. A* **9** (1994) 3841 [Erratum-ibid. *A* **9** (1994) 4353]
doi:10.1142/S0217751X94001552 [hep-th/9306002].
- [6] P. Bowcock, E. Corrigan, P.E. Dorey and R.H. Rietdijk, “Classically integrable boundary conditions for affine Toda field theories”, *Nucl. Phys. B* **445** (1995) 469
doi:10.1016/0550-3213(95)00153-J [hep-th/9501098].
- [7] V.A. Rubakov, “Superheavy magnetic monopoles and proton decay”, *JETP Lett.* **33** (1981) 644 [*Pisma Zh. Eksp. Teor. Fiz.* **33** (1981) 658].
- [8] X.G. Wen, “Chiral Luttinger liquid and the edge excitations in the fractional quantum Hall states”, *Phys. Rev. B* **41** (1990) 12838
doi:10.1103/PhysRevB.41.12838.
- [9] N.D. Antunes, E.J. Copeland, M. Hindmarsh and A. Lukas, “Kink boundary collisions in a two-dimensional scalar field theory”, *Phys. Rev. D* **69** (2004) 065016
doi:10.1103/PhysRevD.69.065016 [hep-th/0310103].
- [10] D.K. Campbell, J.F. Schonfeld and C.A. Wingate, “Resonance structure in kink - antikink interactions in ϕ^4 theory”, *Physica* **9D** (1983) 1
doi:10.1016/0167-2789(83)90289-0.
- [11] M. Peyrard and D.K. Campbell, “Kink antikink interactions in a modified sine-Gordon model”, *Physica* **9D** (1983) 33
doi:10.1016/0167-2789(83)90290-7.
- [12] P. Anninos, S. Oliveira and R.A. Matzner, “Fractal structure in the scalar $\lambda(\phi^2 - 1)^2$ theory”, *Phys. Rev. D* **44** (1991) 1147
doi:10.1103/PhysRevD.44.1147.
- [13] R. Goodman and R. Haberman, “Chaotic scattering and the n-bounce resonance in solitary-wave interactions”, *Phys. Rev. Lett.* **98** (2007) 104103
doi:10.1103/PhysRevLett.98.104103 [arXiv:nlin/0702048].
- [14] P. Dorey, K. Mersh, T. Romanczukiewicz and Y. Shnir, “Kink-antikink collisions in the ϕ^6 model”, *Phys. Rev. Lett.* **107** (2011) 091602
doi:10.1103/PhysRevLett.107.091602 [arXiv:1101.5951 [hep-th]].
- [15] R. Arthur, P. Dorey and R. Parini, “Breaking integrability at the boundary: the sine-Gordon model with Robin boundary conditions”, *J. Phys. A* **49** (2016) no.16, 165205
doi:10.1088/1751-8113/49/16/165205 [arXiv:1509.08448 [hep-th]].
- [16] I.L. Bogolyubsky and V.G. Makhankov, “On the pulsed soliton lifetime in two classical relativistic theory models”, *JETP Lett.* **24** (1976) 12.
- [17] Animations of various aspects of the model can be found at
<https://arxiv.org/src/1508.02329/v2/anc/>.

- [18] T. Romanczukiewicz and Y. Shnir, “Oscillon resonances and creation of kinks in particle collisions”, *Phys. Rev. Lett.* **105** (2010) 081601
doi:10.1103/PhysRevLett.105.081601 [arXiv:1002.4484 [hep-th]].
- [19] T. Sugiyama, “Kink - antikink collisions in the two-dimensional ϕ^4 model”, *Prog. Theor. Phys.* **61** (1979) 1550
doi:10.1143/PTP.61.1550.
- [20] N.S. Manton and H. Merabet, “ ϕ^4 kinks - gradient flow and dynamics”, *Nonlinearity* **10** (1997) 3
doi:10.1088/0951-7715/10/1/002 [hep-th/9605038].
- [21] T. Romanczukiewicz, “Creation of kink and antikink pairs forced by radiation”, *J. Phys. A* **39** (2006) 3479
doi:10.1088/0305-4470/39/13/022 [hep-th/0501066].
- [22] P. Bizoń, T. Chmaj and N. Szpak, “Dynamics near the threshold for blowup in the one-dimensional focusing nonlinear Klein-Gordon equation”, *J. Math. Phys.* **52**, (2011) 103703
doi:10.1063/1.3645363.
- [23] E.J. Copeland, M. Gleiser and H.R. Mueller, “Oscillons: resonant configurations during bubble collapse”, *Phys. Rev. D* **52** (1995) 1920
doi:10.1103/PhysRevD.52.1920 [hep-ph/9503217].
- [24] E.P. Honda and M.W. Choptuik, “Fine structure of oscillons in the spherically symmetric ϕ^4 Klein-Gordon model” *Phys. Rev. D* **65** (2002) 084037
doi:10.1103/PhysRevD.65.084037 [hep-ph/0110065].
- [25] G. Fodor, P. Forgács, P. Grandclément and I. Rácz, “Oscillons and quasi-breathers in the ϕ^4 Klein-Gordon model” *Phys. Rev. D* **74** (2006) 124003
doi:10.1103/PhysRevD.74.124003 [hep-th/0609023].